Supplementary Figures and Supplementary Note to:

Vertebrate kidney tubules elongate using a planar cell polarity-dependent, rosette-based mechanism of convergent extension

Soeren S. Lienkamp[1], Kun Liu[2,5], Courtney M. Karner[3,4], Thomas J. Carroll[3,4], Olaf Ronneberger[2,5], John B. Wallingford[6,7] & Gerd Walz[1,5]

[1]Renal Division, Department of Medicine, University of Freiburg Medical Center, Hugstetter Straße 55, 79106 Freiburg, Germany

[2]Image Analysis Lab, Department of Computer Science, University of Freiburg, Georges-Koehler-Allee 52, 79110 Freiburg, Germany

[3]Department of Internal Medicine, Division of Nephrology, University of Texas Southwestern Medical Center, Dallas, Texas, USA.

[4]Department of Molecular Biology, University of Texas Southwestern Medical Center, Dallas, Texas, USA.

[5]Centre for Biological Signalling Studies (BIOSS), Albertstraße 19, 79104 Freiburg, Germany

[6]Howard Hughes Medical Institute; Section of Molecular Cell and Developmental Biology; University of Texas, Austin, Texas 78712, USA

[7]Institute for Cellular and Molecular Biology, University of Texas, Austin, Texas 78712, USA
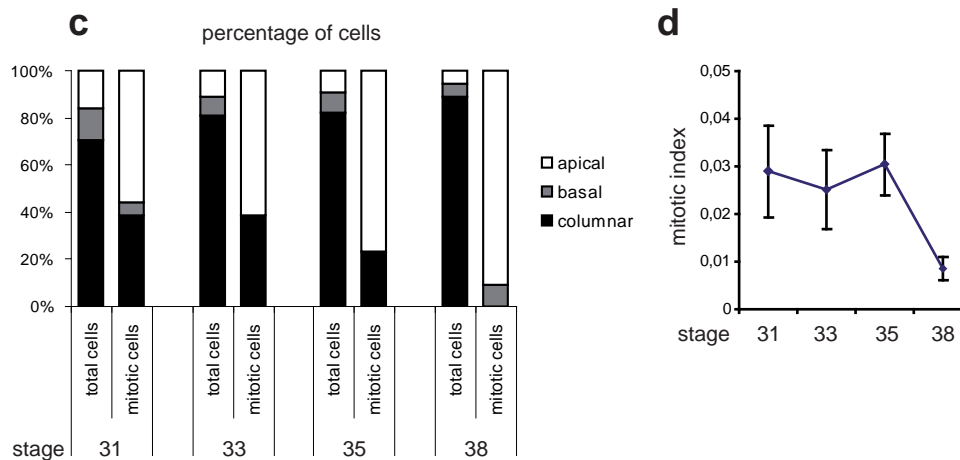
Correspondence should be addressed to J.B.W (wallingford@mail.utexas.edu), or G.W. (gerd.walz@uniklinik-freiburg.de).
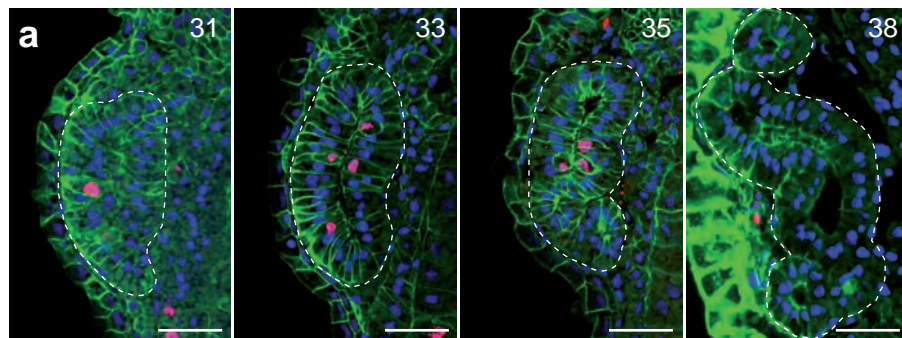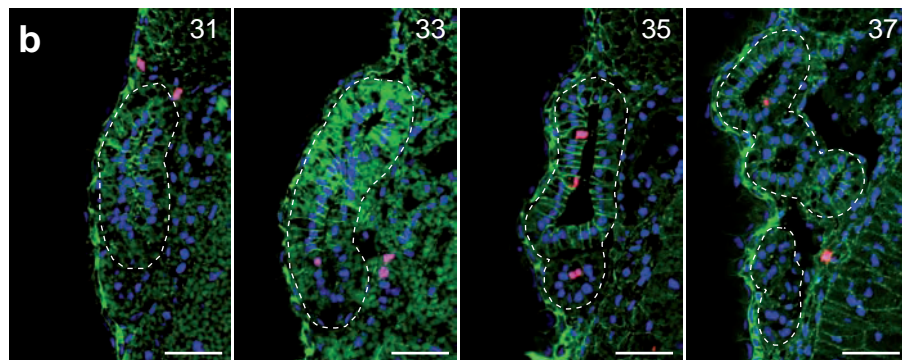
**Suppl. Figure 1 Lumen formation and apical mitosis in the Xenopus pronephros**
Lumen formation begins around stage 35. Xenopus embryos, expressing membrane-associated GFP (memGFP), were fixed at indicated stages with anti-phopsho-histone-H3 (p-Histone-H3) and DAPI in combination with either **(a)** anti-GFP or **(b)** anti-β-catenin before sectioning (5µm plastic sections). The pronephros is outlined by a broken line. Scale bar, 50 µm. **(c)** Cells were classified by position within the epithelium. Apical and basal cells do not reach the opposing epithelial side, while columnar shaped cells extent from the basal side to the apical surface. Increasing numbers of mitotic cells are found at the apical side as development progresses, indicative of a pseudo-stratified epithelium. **(d)** The mitotic index declines towards stage 38 (error bars, SEM). A total of 7-8 embryos were analyzed for each stage.
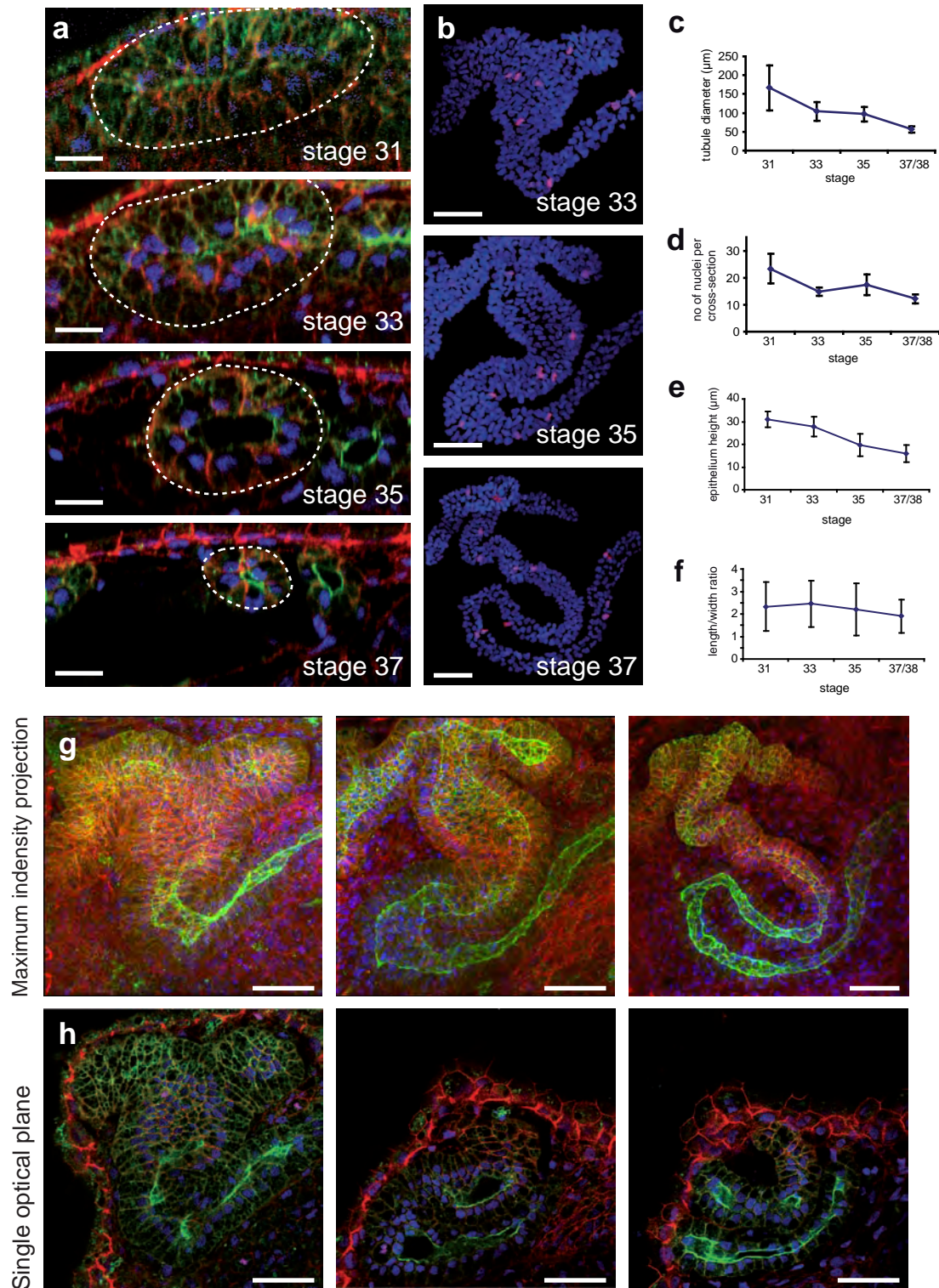
Suppl. Figure 2 The tubule diameter decreases as fewer cells form the tubule diameter
Confocal stacks of Xenopus embryos were stained with anti-β-catenin (red), tomato-lectin (green) and DAPI (blue), and anti-phospho-histone H3 (purple). **(a)** Optical cross-sections were positioned perpendicular to the tubule of the proximal segment at indicated stages. The tubules are outlined by white broken lines. Scale bar, 20 µm. **(b)** Mitotic cells (red) are found in all segments. Scale bar 50 µm. **(c)** Decrease of tubular diameter over time. **(d)** Decreasing number of cells per diameter. **(e)** The epithelium flattens during development. **(f)** The length-width ratio of tubule epithelial cells remains constant. Error bars for all graphs: SEM **(g)** Maximum intensity projections of images in Fig. 2b,c,d without cell rendering. **(h)** Single optical planes to visualize cell boundaries that were used to 3D render cells in Fig. 2b,c,d. Scale bar, 50 µm.
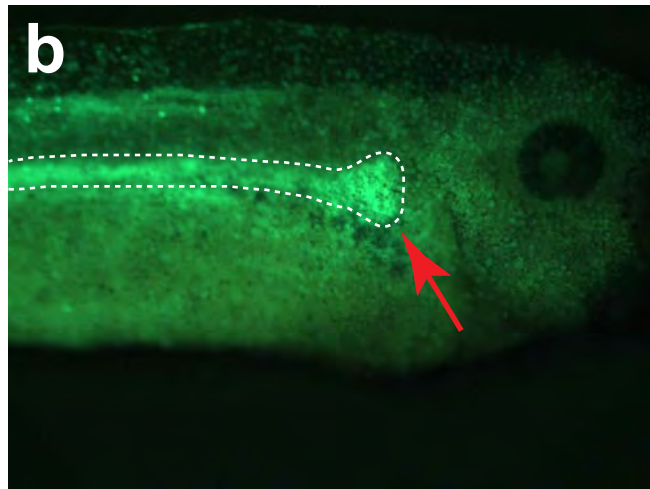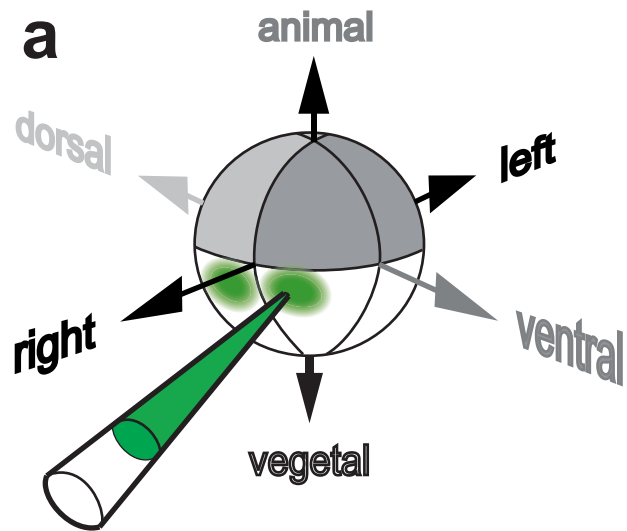
Suppl. Figure 3 Targeted injection for tissue limited expression of fluorescent proteins
**(a)** Schematic depiction of a Xenopus embryo at the 8-cell stage. Injections were performed into the lateral-vegetal blastomeres. **(b)** Expression of GFP is predominantly limited to the pronephros of the stage 36 tadpole (outlined by a broken line, red arrow).
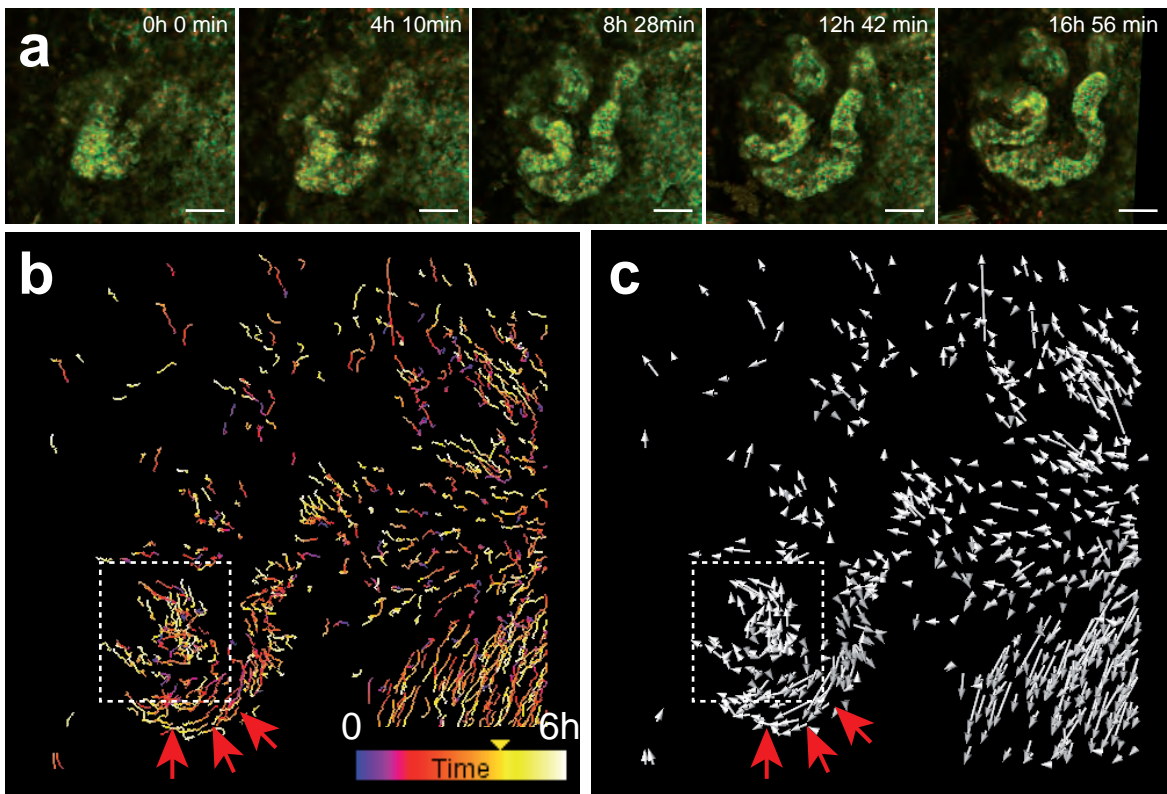
Suppl. Figure 4 Time-lapse imaging of pronephros morphogenesis
(a) Maximum intensity projections of confocal time-lapse recordings after expression of membrane-GFP and histone H3-RFP in the Xenopus pronephros is shown for the duration of 16 hours and 56 minutes. Scale bar, 100 μm. **(b)** Automated detection and tracking of nuclei was performed to visualize morphogenetic movements. Time-coded movement tracks of single nuclei reveal the cell movements during renal tubule development. **(c)** Displacement vectors indicate the start and ending postion of tracks in (b) independent of velocity. The complex cell rearrangements during tubule narrowing of the proximal tubule (white broken box) are highlighted. Red arrows highlight anterior movement of cells in the intermediate segment.
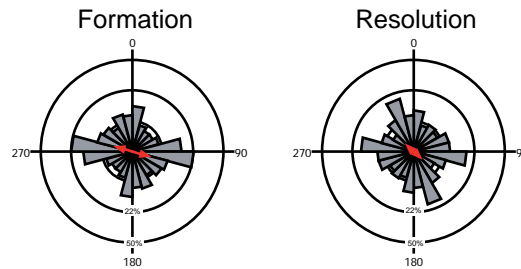
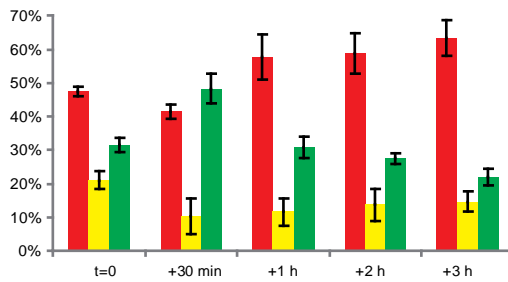**a** Tissue elongation by remodelling of 4-cell junctions

Type 1 → Type 2 → Type 3
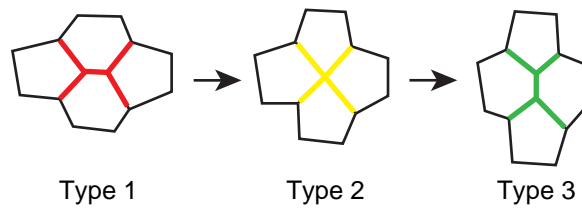
b Proportion of 4-cell junctions over time
WT (n=3 tubules)

Type 1
Type 2
Type 3
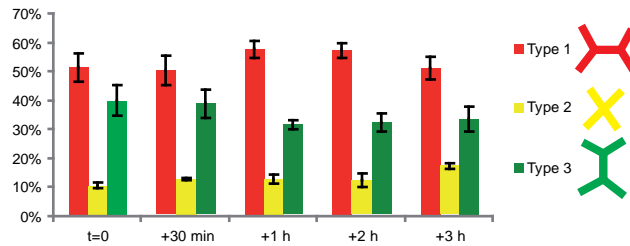
c Wild type Type 2 Junction

Formation   Resolution
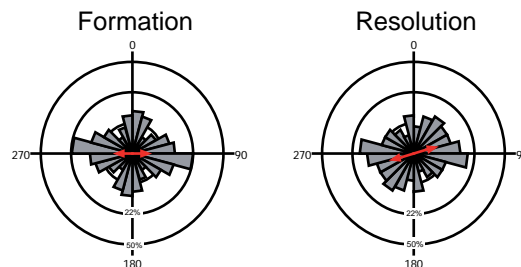
d Proportion of 4-cell junctions over time
Xdd1-GR (n=3 tubules)

e Xdd1-GR Type 2 Junction

Formation   Resolution

Suppl. Figure 5 The formation and resolution of 4-cell junctions is not polarized
(a) Diagram of a potential tissue elongation mechanism based on 4-cell remodeling. **(b)** Distribution of type 1, 2 and 3 junctions over time in wild type and **(c)** The angular distribution of formation and resolution of type 2 junctions is not significantly biased (p=0,4, Mardia-Watson-Wheeler test, n= 90 type-2 junctions in 3 tubules). **(d)** Xdd1-GR expressing tubules (n=3 tubules). Type 1 junctions are horizontally aligned to the longitudinal axis of the tubule. Type 2 junctions of 4 meeting cells. Type 3 junctions are vertically aligned. No progression towards type 3 junctions is observed. **(e)** The resolution angle of Xdd1-GR expressing tubules. (p=0.6, n= 46 type-2 junctions in 3 tubules). Red arrows indicate the mean angle.
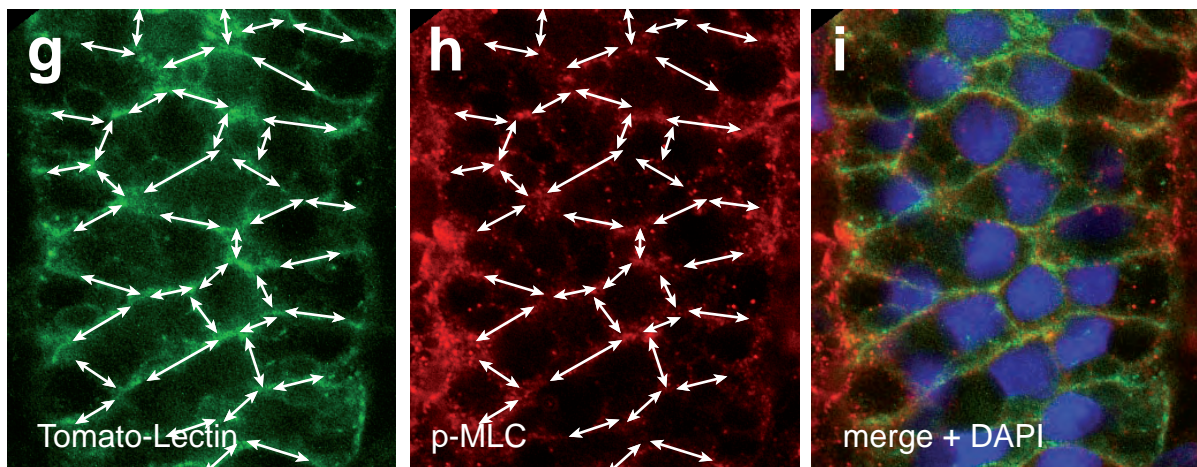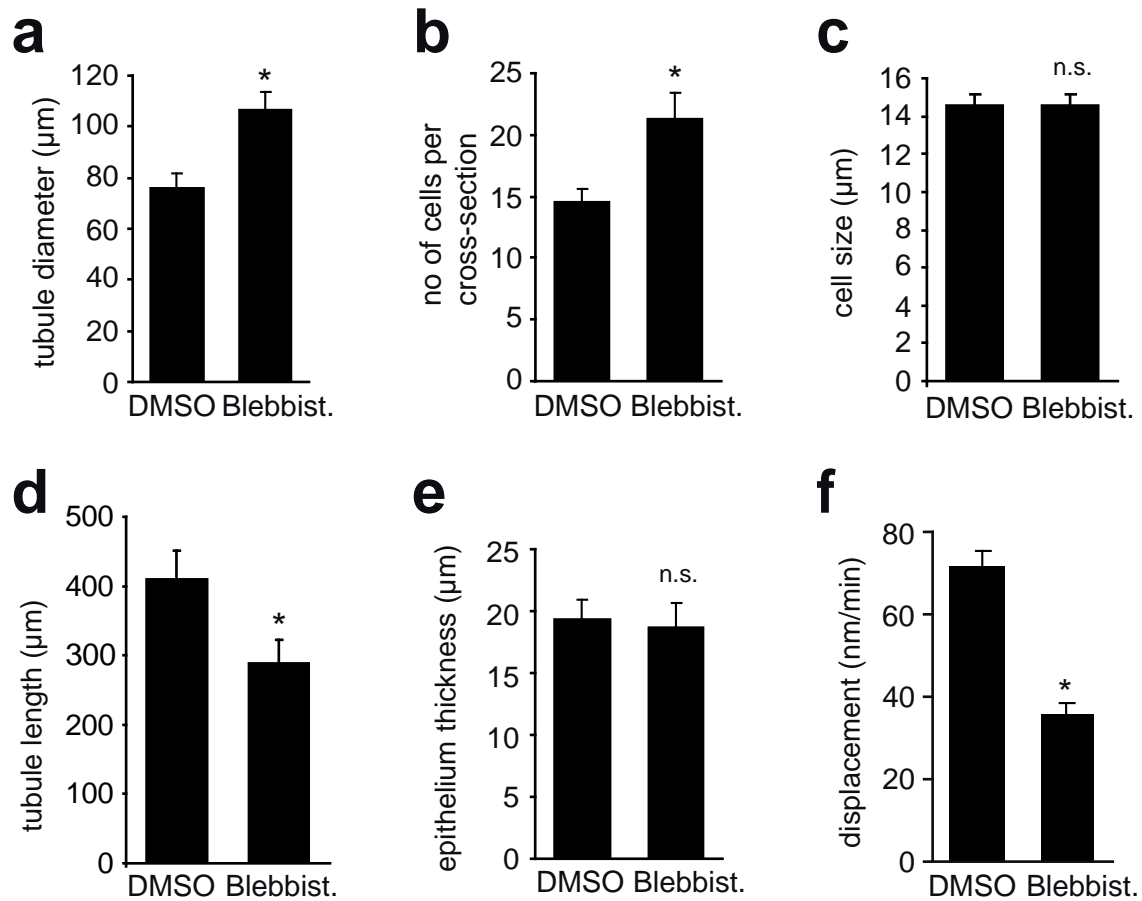
Suppl. Figure 6 Blebbistatin treatment has profound effects on tubule morphogenesis and rosette formation: (a) The tubule diameter is enlarged after treatment with blebbistatin (Blebbist.). (b) The number of cells contributing to the tubule circumference is increased. (c) Cell size, measured as the maximum diameter of the basal surface in mediolateral direction is not significantly different. (d) Tubule length was determined from the confluence of the nephrosomes to the anterior part of the intermediate segment (see yellow line in Fig.4a,b) and is significantly reduced. (e) The epithelium thickness is unchanged in blebbistatin treated embryos. (n.s. not significant, *p < 0.05, t-test, n=13 DMSO treated embryos, n=16 blebbistatin treated embryos.) (f) the displacement speed is significantly reduced in tracked cells (*p<0.01; DMSO: n=161; blebbistatin: n=176 cells in 3 parallel imaged embroys; error bars: SEM in all graphs). (g) Xenopus embryos were stained for phosphor-Myosin light chain, and Tomato lectin (h) visualizing the cell membranes in renal tubules. Arrows indicate where intensity measurements were taken. The angles were taken in relationship to the tubular lumen. (proximal to the top and distal to the bottom). (i) Merged image of (g) and (h) including the DAPI channel.

a Multi-cellular rosettes in wildtype and Wnt9b mutant mouse kidneys

b Multi-cellular rosettes in wildtype and Xdd1-GR *Xenopus* kidneys
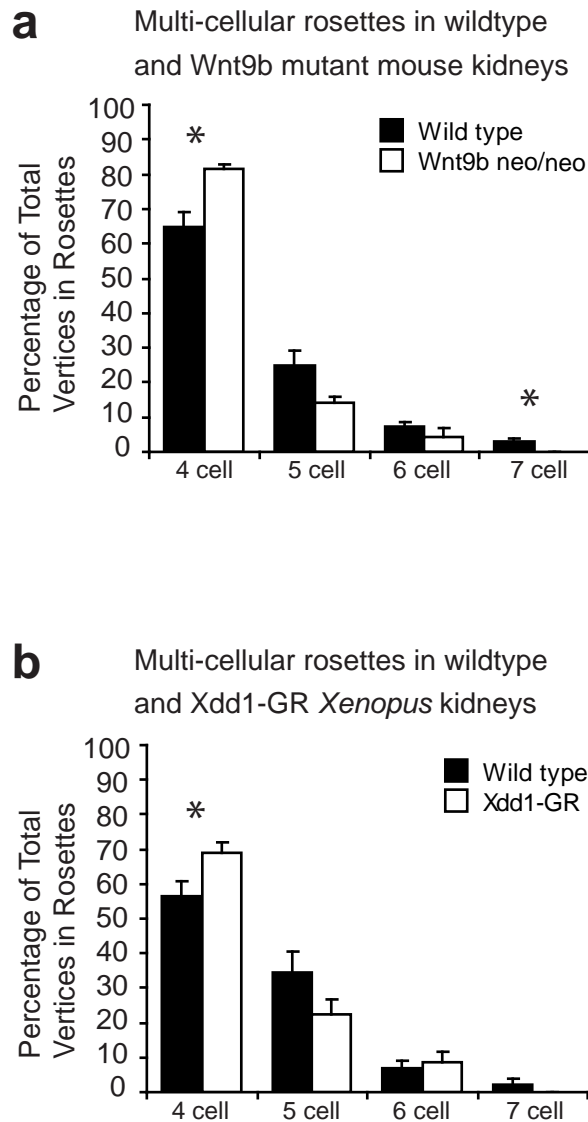
Suppl. Figure 7 Rosette formation in Wnt9b deficient mice and Xdd1 expressing Xenopus tubules
(a) The quantitative analysis of the number of cells participating in rosette formation reveals a shift towards lower order rosettes in Wnt9bneo/neo kidneys in comparison to wild type kidneys. (Wnt9bneo/neo: n=212 rosettes; wild type: n=263 rosettes in 3 embryos, *p<0.05, t-test, error bars: SEM) **(b)** The quantitative analysis of rosettes in fixed Xenopus renal tubules at stage 37 reveals a similar shift towards lower order rosettes in Xdd1-GR expressing kidneys (Xdd1-GR: n=97 rosettes, wild type: n= 96 rosettes in 7 embryos; *p < 0.05, t-test, error bars: SEM).
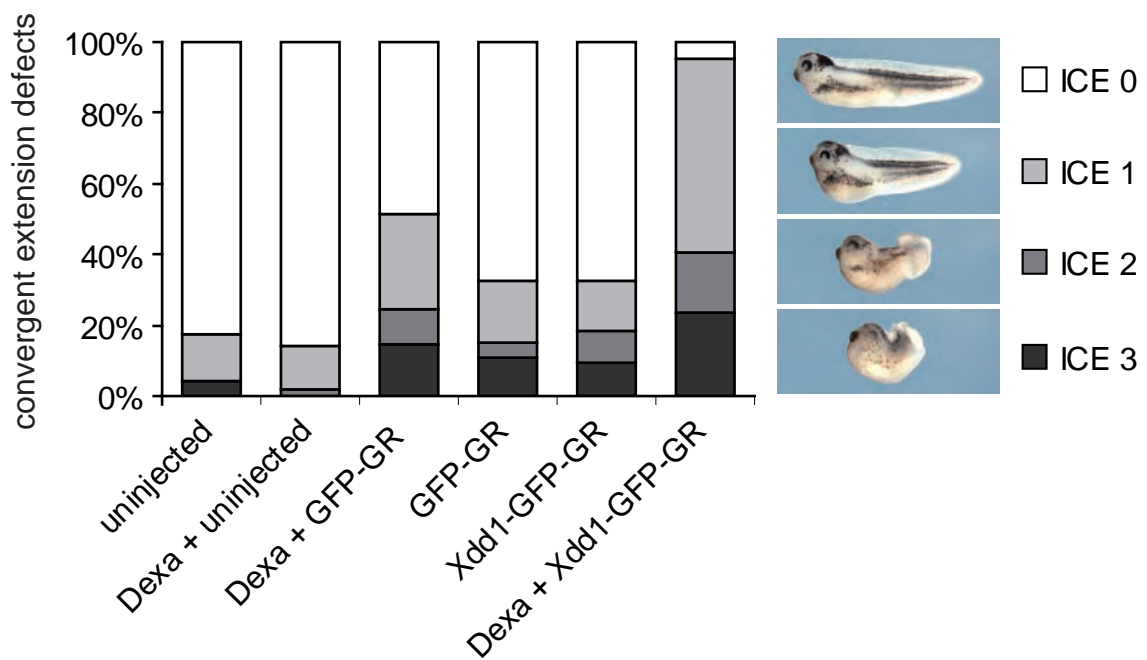
Suppl. Figure 8 Effect of Xdd1-GR expression on convergent extension.
Both dorsal blastomeres of Xenopus embryos were injected at the 4-cell stage with RNA coding for a fusion protein of Xdd1 and the human growth-hormone receptor (Xdd1-GR). The shortened axis scored as depicted at stage 36-40 (ICE: impaired convergent extension). In the presence of dexamethasone (Dexa, activating hormone of Xdd1-GR) the defects were strongest, while dexamethasone treatment alone had no effect on development of Xenopus embryos (n= 41 to 49 embryos in each group) .
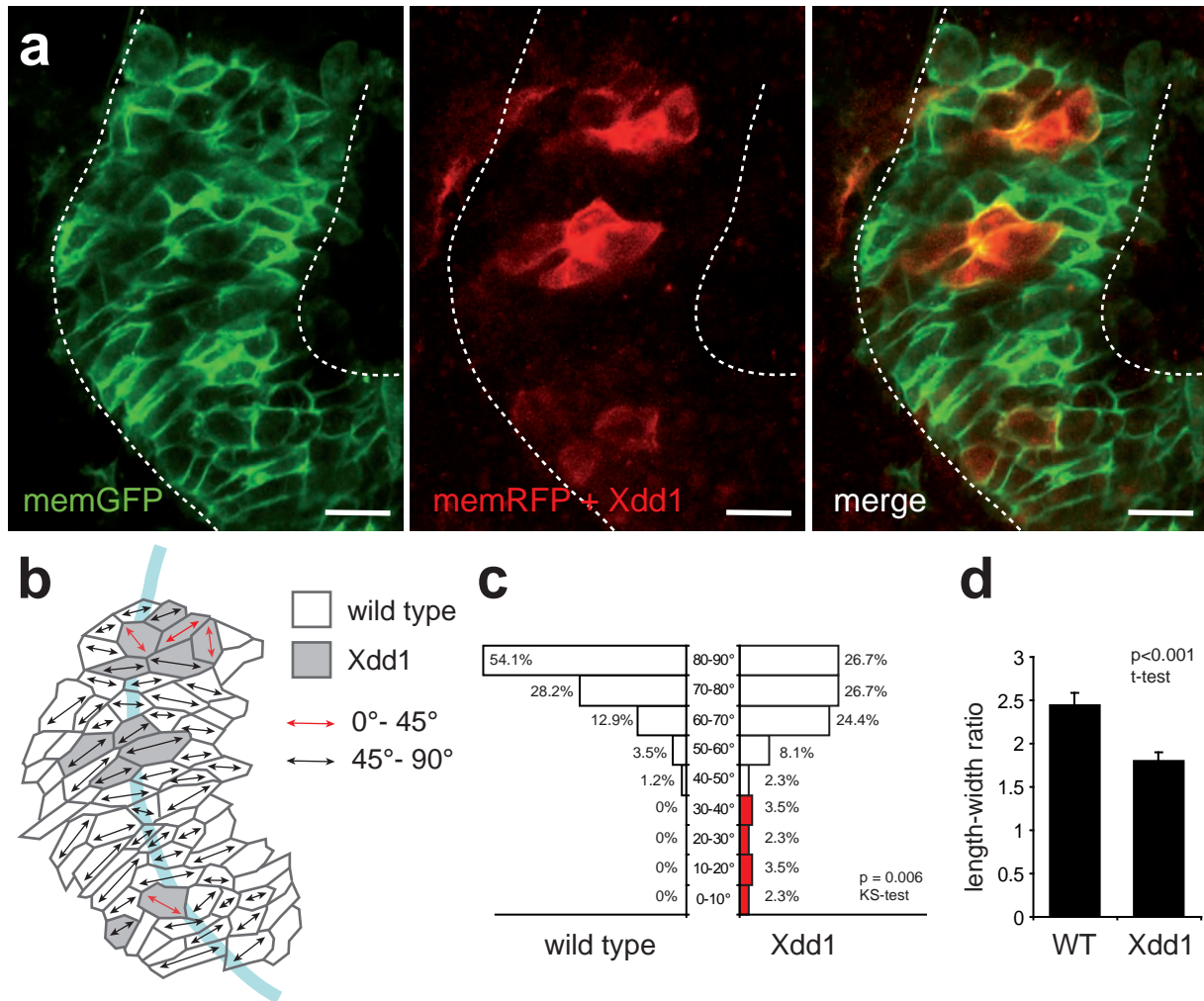
Suppl. Figure 9 Cell elongation and orientation is influenced by Xdd1

(a) Xdd1, a dominant-negative Dishevelled mutation that specifically interferes with planar cell polarity signaling, is expressed in a subset of tubular epithelial cells labeled by membrane-associated RFP (memRFP, red) in Xenopus embryos. All other tubular epithelial cells (wild type) are marked by membrane-associated GFP (memGFP, green). Scale bar, 20 µm. **(b)** The angle of the longest cell diameter was measured. Red arrows indicate and angle in relationship to the longitudinal axis of the tubule (blue line) between 0 and 45°; a gray arrow labels cells with an angle between 45 and 90°. **(c)** The distribution of angles reveals that more Xdd1-expressing cells are oriented in angles <45° in relationship to the tubule axis (wild type cells, n=85 measurements at hourly intervals of 19 cells; Xdd1-positive cells, n=86 measurements of 20 cells; p=0.006). **(d)** The length-width ratio is decreased by Xdd1 (p<0.001, t-test, error bars: SEM).
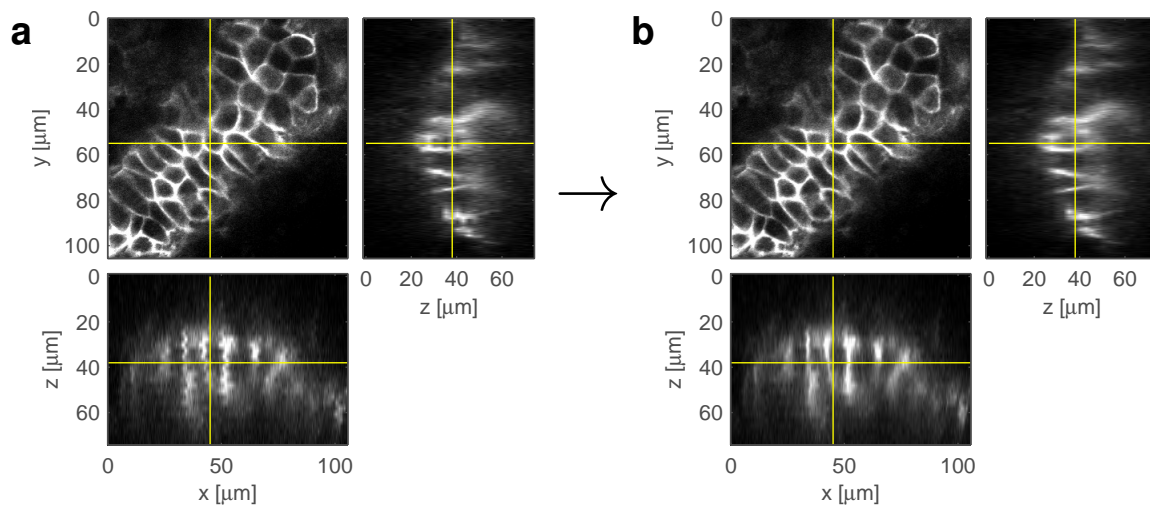
Supplementary Figure 10 │ Heart beat compensation: (**a**) Raw data shows significant artefacts due to fast pulsation of the sample during confocal scanning (most notable here in the xz-slice). (**b**) After compensation by elastic registration of subsequent slices these artefacts are removed
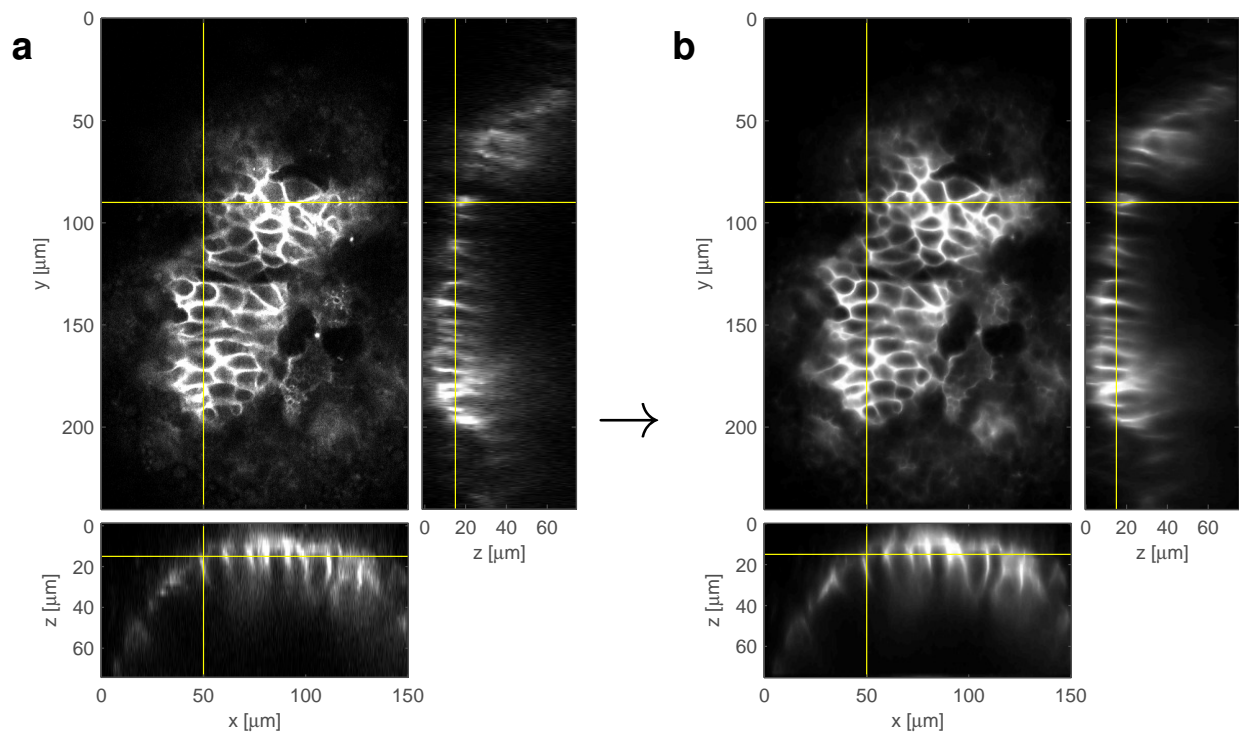
Supplementary Figure 11 | Anisotropic diffusion for cell border enhancement and denoising: (**a**) raw data, (**b**) filtered data
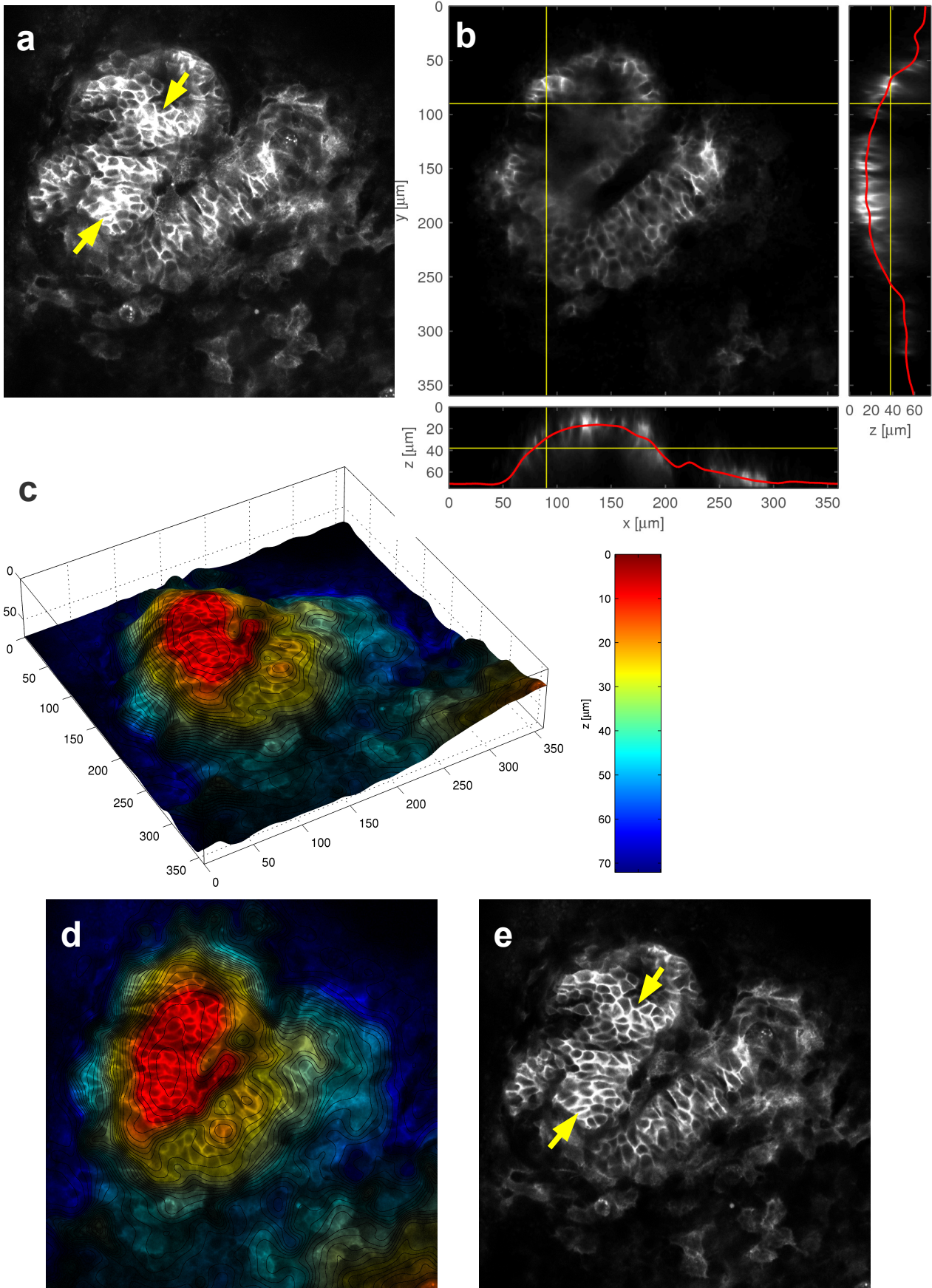
Supplementary Figure 12 │ Cell layer extraction: (**a**) Maximum intensity projection of raw image stack. (**b**) Orthogonal slices of filtered image stack. The red lines indicate the detected cell layer. (**c**) 3D rendering of the extracted cell layer. The color and the contour lines depict the z-position in the data set. (**d**) Extracted slice with color code and contour lines. (**e**) Extracted slice for further processing. Cell borders are clearly visible.
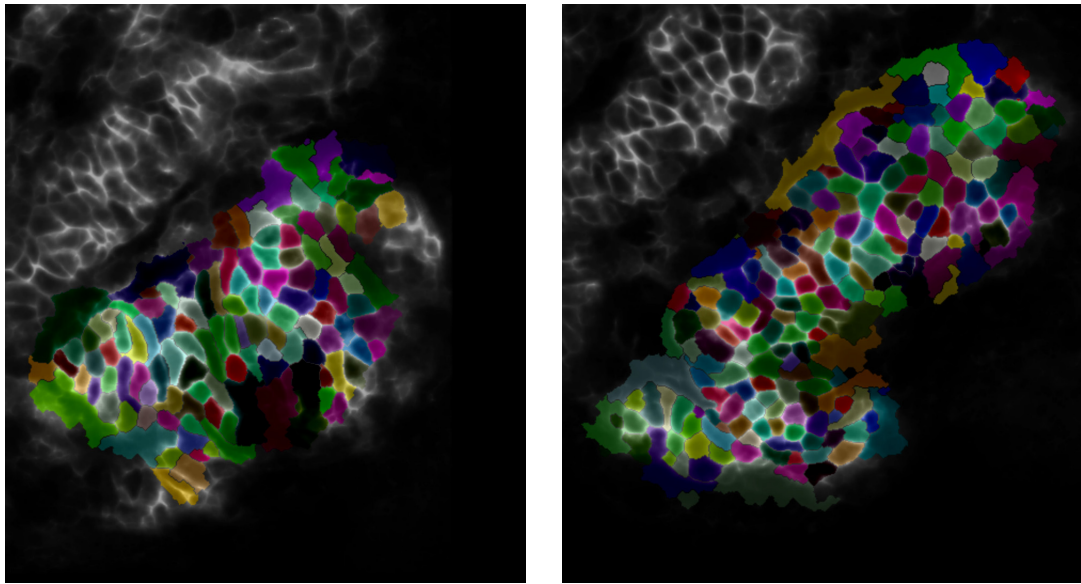
Supplementary Figure 13 │ Automatic cell segmentation: two frames of random-colored segmentation masks overlaid on the enhanced images. This result comes from a marker-controlled watershed and the voting from neighboring frames, which are aligned based on the optical flow.
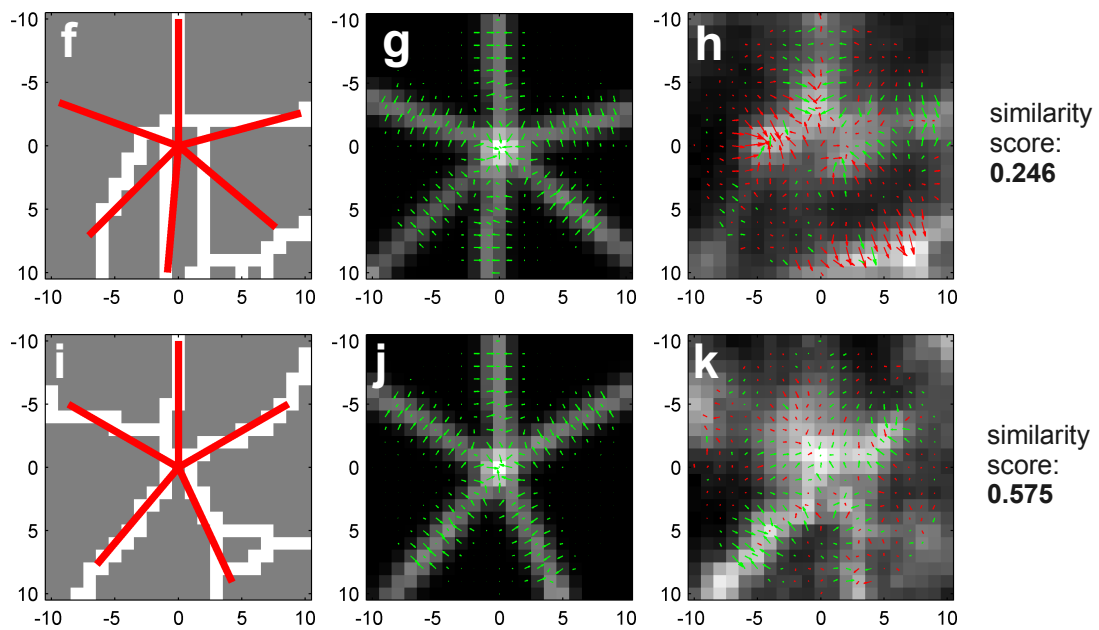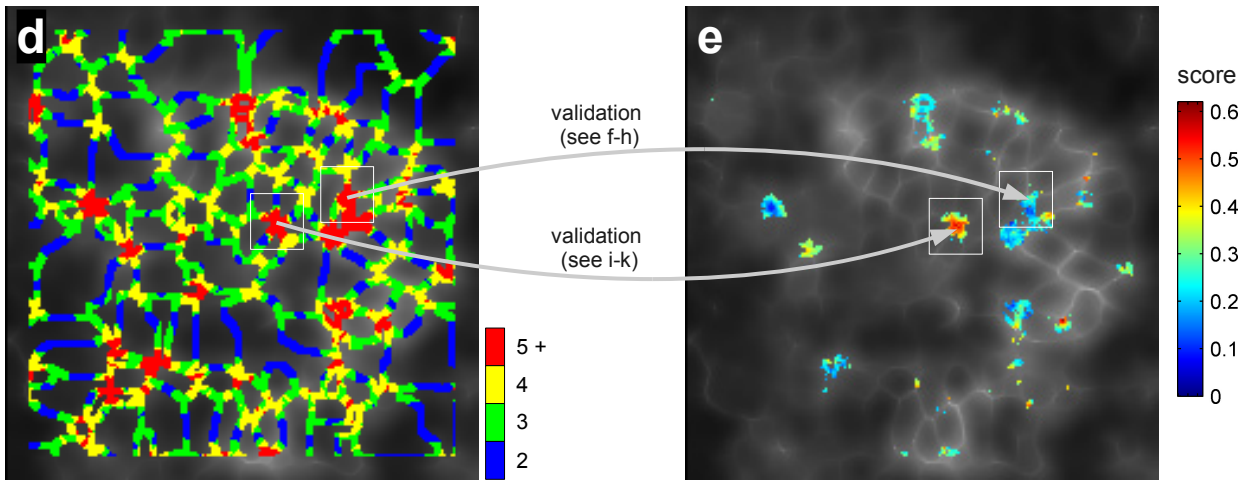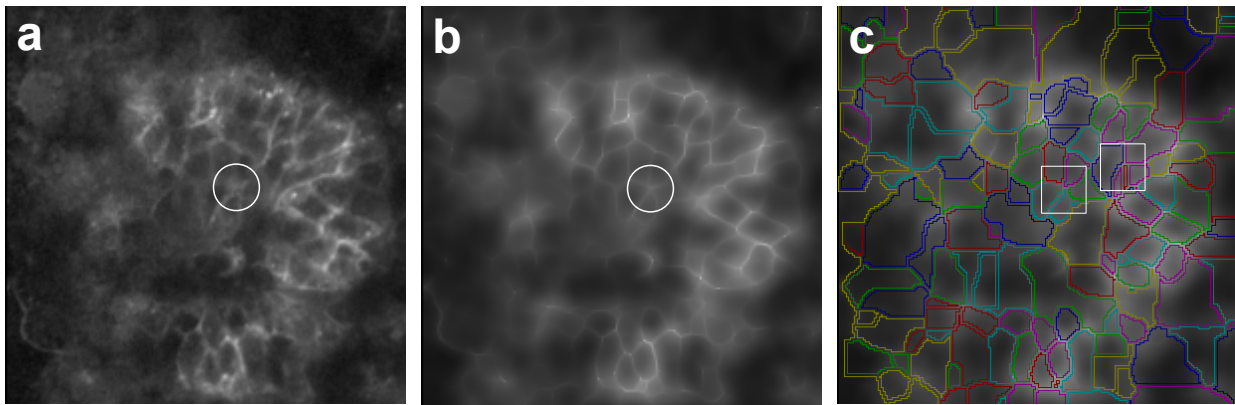
Supplementary Figure 14 │ Rosette Detection: (**a**) Cell layer extracted from raw image. (**b**) Cell layer extracted from filtered image. (**c**) Over-segmentation by watershed. Two rosette center candidates are depicted by white squares (**d**) Rosette center candidates. The color indicates the number of segments in the surrounding. Two of these candidates are depicted by a white square (**e**) Final detection score after validation. (**f-k**) Validation of candidates with the star-shaped rosette model: (**f**) Best fitting rosette model, given the watershed lines. (**g**) Synthetic rosette image. Gradient vectors are overlaid in green (**h**) Raw image at validation position. Gradient vectors of raw image are shown in red and green, where green indicates a match of the gradient direction with the synthetic image. (**i-k**) Analog images as in f-h but for a different position.

Supplementary Note

Notation

Images are denoted as continuous functions that map a given coordinate to the intensity at this point. Usually, 2D images are defined on a rectangular-shaped domain $\Omega \subset \mathbb{R}^2$ and 3D (volumetric) images are defined on a cuboid shaped domain $\Omega \subset \mathbb{R}^3$. A typical example for an Image is $I : \Omega \to \mathbb{R}; \mathbf{x} \mapsto I(\mathbf{x})$ with $\mathbf{x} \in \Omega$ and $I(\mathbf{x}) \in \mathbb{R}$.

Heart Beat Compensation

The confocal microscope scans the sample line-by-line and plane-by-plane. Therefore the time difference of two neighboring pixels in x-direction is in the range of microseconds, in y-direction in the range of milliseconds and in z-direction in the range of seconds (assuming an image size of approx. 1000x1000 in xy-direction). As the heart beat frequency is approx. 2-3 beats per second, the periodic deformations produce severe discontinuities of the structures in z-direction (Supplementary Fig. 10a). We compensate the discontinuities by an elastic deformation of each slice: For this, the image stack is described by a set of N 2D slices $S_i : \mathbb{R}^2 \to \mathbb{R}; \mathbf{x} \mapsto S_i(\mathbf{x}); i \in \{1, \ldots, N\}$. For each pair of subsequent slices the pixel correspondences are found by a dense diffeomorphic registration [1], such that

$$S_i(\mathbf{x}) = S_{i+1}(\mathbf{x} + \mathbf{F}_i(\mathbf{x})), \tag{1}$$

where $\mathbf{F}_i : \mathbb{R}^2 \to \mathbb{R}^2; \mathbf{x} \mapsto \mathbf{F}_i(\mathbf{x})$ is the forward deformation field. Due to the diffeomorphism the inverse deformation $B_{i+1} := F_i^{-1}$ always exists. We denote the backward deformation field as $\mathbf{B}_i : \mathbb{R}^2 \to \mathbb{R}^2; \mathbf{x} \mapsto \mathbf{B}_i(\mathbf{x})$, such that

$$S_i(\mathbf{x}) = S_{i-1}(\mathbf{x} + \mathbf{B}_i(\mathbf{x})). \tag{2}$$

After all F_i and B_i are computed for each pair of slices, the relation of three subsequent slices can be written as

$$S_{i-1}(\mathbf{x} + \mathbf{B}_i(\mathbf{x})) = S_i(\mathbf{x}) = S_{i+1}(\mathbf{x} + \mathbf{F}_i(\mathbf{x})). \tag{3}$$

The optimal deformation $\mathbf{U}_i : \mathbb{R}^2 \to \mathbb{R}^2$ for each slice (considering the two neighboring slices) is found by applying a small filter with the kernel $K = (\frac{1}{4}, \frac{1}{2}, \frac{1}{4})$ to the displacements. The displacement of the slice S_i to itself is zero, so the optimal resulting deformation field is:

$$\mathbf{U}_i(\mathbf{x}) = \frac{1}{4}\mathbf{F}_i(\mathbf{x}) + \frac{1}{4}\mathbf{B}_i(\mathbf{x}). \tag{4}$$

To corrected slice is then

$$S_{\text{corrected},i}\left(\mathbf{x} + \mathbf{U}_i(\mathbf{x})\right) = S_i(\mathbf{x}). \tag{5}$$

The result is shown in Supplementary Fig. 10b.

Cell border enhancement and Denoising

The anisotropic diffusion for cell border enhancement and denoising can be formulated in this partial derivative equation [5]:

$$\frac{\partial I(\mathbf{x})}{\partial t} = \text{div}(\mathbf{D}(\mathbf{x})\nabla I(x)), \tag{6}$$

where ∇ indicates the gradient of image, and div is the divergence. The diffusion behavior is controlled by the diffusion tensor $\mathbf{D} : \Omega \to \mathbb{R}^{3\times3}; \mathbf{x} \mapsto \mathbf{D}(\mathbf{x})$. The diffusion result after a certain time can be computed by an explicit time integral. It is well-known that the Hessian matrix (second-order derivatives) is very effective for featuring plan-like structures [4], so it is used here to construct the diffusion tensor, which drives the diffusion

process in the anisotropic way. Let the eigenvalues of the local Hessian matrix be $\ell_1 > \ell_2 > \ell_3$, and their corresponding eigenvectors be $\mathbf{v}_1, \mathbf{v}_2, \mathbf{v}_3$, then the diffusion tensor is constructed as

$$\mathbf{D} = e^{-(\min(\ell_1,0)/\kappa)^2}\mathbf{v}_1\mathbf{v}_1^T + e^{-(\min(\ell_2,0)/\kappa)^2}\mathbf{v}_2\mathbf{v}_2^T + e^{-(\min(\ell_3,0)/\kappa)^2}\mathbf{v}_3\mathbf{v}_3^T. \tag{7}$$

The parameter κ is optimized manually to obtain clear cell borders within the tubule structures. The effect of this diffusion tensor can be explained as follows: it suppresses the diffusion along the directions in which ℓ is large compared to κ (which means there is a bright border), and allows strong diffusion along the directions in which there are no clear border. The effect of the enhancement is illustrated in Supplementary Fig. 11.

Cell layer extraction

The local z-position of the curved single cell-layer (Supplementary Fig. 12b-e) is estimated in the filtered image by searching the position with the sharpest edges (highest gradient magnitude) while keeping the layer smooth. The filtered volumetric image is denoted as $I : \mathbb{R}^3 \to \mathbb{R}$. The edge score $E : \mathbb{R}^3 \to \mathbb{R}$ is computed from the x and y component of the gradient as

$$E(x,y,z) = \sqrt{\left(\frac{\partial}{\partial x}I\right)^2(x,y,z) + \left(\frac{\partial}{\partial y}I\right)^2(x,y,z)}. \tag{8}$$

Then the edge information (originating mainly from the cell borders) is spread into the local surrounding by filtering with a "flat" Gaussian kernel

$$G_1(x,y,z) = e^{-\left(\frac{x^2+y^2}{\sigma_{xy}^2} + \frac{z^2}{\sigma_z^2}\right)}, \tag{9}$$

with $\sigma_{xy} = 15\mu m$ and $\sigma_z = 2\mu m$. Finally the z-position of the maximal score is determined for each (x,y) position,

$$Z_{\text{opt}}(x,y) = \arg\max_z (G_1 * E)(x,y,z), \tag{10}$$

and filtered with a Gaussian kernel G_2 with $\sigma_{xy} = 15\mu m$ to obtain a smooth shape without jumps in z-direction:

$$Z_{\text{final}}(x,y) = (G_2 * Z_{\text{opt}})(x,y) \tag{11}$$

The extracted cell layer $S : \mathbb{R}^2 \to \mathbb{R}$ is then

$$S(x,y) = I\left(x,y,Z_{\text{final}}(x,y)\right). \tag{12}$$

Drift Compensation (Stabilization)

The displacement of two successive data sets $I_t : \mathbb{R}^3 \to \mathbb{R}$ and $I_{t+1} : \mathbb{R}^3 \to \mathbb{R}$ is estimated by a normalized cross correlation of their maximum intensity projections $M_t : \mathbb{R}^2 \to \mathbb{R}$ and $M_{t+1} : \mathbb{R}^2 \to \mathbb{R}$.

$$N_{\text{CC},t}(\mathbf{d}) = \frac{\int_\Omega \left(M_t(\mathbf{x}) - \overline{M_t} \right) \cdot \left(M_{t+1}(\mathbf{x} + \mathbf{d}) - \overline{M_{t+1}}(\mathbf{d}) \right) d\mathbf{x}}{\sqrt{\left(\int_\Omega \left(M_t(\mathbf{x}) - \overline{M_t} \right)^2 d\mathbf{x} \right) \cdot \left(\int_\Omega \left(M_{t+1}(\mathbf{x} + \mathbf{d}) - \overline{M_{t+1}}(\mathbf{d}) \right)^2 d\mathbf{x} \right)}} \tag{13}$$

with

$$\overline{M_t} := \frac{1}{|\Omega|} \int_\Omega M_t(\mathbf{x}) d\mathbf{x} \tag{14}$$

$$\overline{M_{t+1}}(\mathbf{d}) := \frac{1}{|\Omega|} \int_\Omega M_{t+1}(\mathbf{x} + \mathbf{d}) d\mathbf{x} \,. \tag{15}$$

The best displacement is determined by the maximum of N_{CC} as

$$\mathbf{d}_{\text{best},t} = \arg\max_{\mathbf{d}} N_{\text{CC},t}(\mathbf{d}) \,. \tag{16}$$

The stabilization of the whole time series is then performed by transforming each frame $S_t : \mathbb{R}^2 \to \mathbb{R}$ with the cumulated displacements,

$$S_{\text{stab},t}(\mathbf{x}) = S_t \left(\mathbf{x} + \sum_{i=1}^{t-1} \mathbf{d}_{\text{best},i} \right) \,. \tag{17}$$

Semi-automated Cell Tracking

The cell tracking is performed on the stabilized cell layer slices $S_{\text{stab},t} : \Omega \to \mathbb{R}$, with $\Omega \subset \mathbb{R}^2$ and $t \in \{1, \ldots, T\}$, that were extracted from the filtered images. The cell centers in the last frame $S_{\text{stab},T}$ are found by searching for local gray value minima

$$\mathcal{M} = \left\{ \mathbf{x} \in \Omega : S_{\text{stab},T}(\mathbf{x}) < S_{\text{stab},T}(\mathbf{n}) \wedge 0 < \|\mathbf{n} - \mathbf{x}\| \leq \sqrt{2}g \quad \forall \mathbf{n} \in \Omega \right\} \,, \tag{18}$$

where $g \in \mathbb{R}$ denotes the pixel grid spacing in micrometer. To avoid double detections of the same cell, minima that are closer to a stronger minimum than the minimal cell diameter (here 4μm) are removed. The potiential double detections of each detection x are denoted as

$$\mathcal{D}(\mathbf{x}) = \left\{ \mathbf{y} \in \mathcal{M} : 0 < \|\mathbf{y} - \mathbf{x}\| \leq 4\mu\text{m} \right\} \,. \tag{19}$$

Then we can write the set of final detections as

$$\mathcal{M}' = \left\{ \mathbf{x} \in \mathcal{M} : \mathcal{D}(\mathbf{x}) = \emptyset \vee \left(S_{\text{stab},T}(\mathbf{x}) < S_{\text{stab},T}(\mathbf{n}) \quad \forall \mathbf{n} \in \mathcal{D}(\mathbf{x}) \right) \right\} \,. \tag{20}$$

The tracking uses the backward optical flow. For the high quality datasets with low variation in the intensities the high accuracy optical flow [2] is used. For the datasets with greater variations in the image intensities a slightly less accurate but more robust method [1] using the locally normalized cross correlation as similarity measure was used for the flow computation.

The backward flow is denoted as $\mathbf{b}_t : \mathbb{R}^2 \to \mathbb{R}^2$. Each cell center is tracked back in time by searching for the trajectory that gives the best compromise between following the dense optical flow and passing through

the local gray value minima. The energy for a single trajectory, described by the position $\mathbf{x}_t$ for every time point is

$$E(\mathbf{x}_1, \ldots, \mathbf{x}_T) = \sum_{t=1}^{T-1} \left(\mathbf{x}_t - \left(\mathbf{x}_{t+1} + \mathbf{b}_{t+1}(\mathbf{x}_{t+1}) \right) \right)^2 + \lambda S_{\text{stab},t}(\mathbf{x}_t). \tag{21}$$

The parameter λ controls the relative weight the optical flow (term 1) and the image intensities (term 2). The global optimum of this energy is computed using dynamic programming and the fast squared distance transform of Felsenszwalb and Huttenlocher [3]. The global optimum over the whole time series often does not correspond to the correct cell trajectory, because only a few cells are visible in all frames. Therefore the energy was optimized piecewise, and superfluous parts of the trajectories were removed in a subsequent manual editing step. In a final validation step, all trajectories were manually inspected and corrected, if necessary.

Rosette Detection

The rosette center candidate are found in an over-segmented image (see Online Methods and Supplementary Fig. 14c). For all rosette center candidates, the surrounding image patch $P : \mathbb{R}^2 \to \mathbb{R}$ (extracted from the raw image) is compared to a rosette model that consists of five (or more) radial rays with a length of $R = 7.5\mu$m. This comparison is performed in two steps. In the first step the model parameters (angle of each ray) are determined as local maxima of the radial intensity sum of the watershed line image W (see Supplementary Fig. 14f and i)

$$p(\varphi) = \int_0^R W(\varphi, r) \, dr \tag{22}$$

$$\mathcal{A} = \{\varphi \mid p'(\varphi) = 0 \wedge p''(\varphi) < 0\}. \tag{23}$$

To remove double detections of a single cell wall, all detections that are closer than $\varphi_{\min} = 30°$ to a neighboring stronger detection are removed:

$$\mathcal{A}_{\text{final}} = \{\varphi \mid \varphi \in \mathcal{A}; \ \beta \in \mathcal{A}; \ |(\varphi - \beta) \bmod 2\pi| > \varphi_{\min} \ \vee \ p(\varphi) > p(\beta)\}. \tag{24}$$

Using the angles in the set $\mathcal{A}_{\text{final}}$ a synthetic image patch $M : \mathbb{R}^2 \to \mathbb{R}$ is rendered by drawing the rays and smoothing them with a Gaussian kernel G_3 with $\sigma = 0.75\mu$m (Supplementary Fig. 14g and j)

$$L(\varphi, r) = \begin{cases} 1 & \text{if } \varphi \in \mathcal{A}_{\text{final}} \wedge r \leq R \\ 0 & \text{else} \end{cases} \tag{25}$$

$$M = G_3 * L. \tag{26}$$

Finally the synthetic and the real image patch are compared using a gradient based similarity metric that is robust to local intensity variations and additional small structures(Supplementary Fig. 14h and k). For this, we define the circular mask as $\Omega_c = \{\mathbf{x} \in \mathbb{R}^2 \mid \|\mathbf{x}\| \leq R\}$, and specify a maximal angle between gradient vectors $\alpha_{\max}$ (here we use $\alpha_{\max} = 45°$). With the following definitions

$$P_{\text{gmag}} := \|\nabla P\| \qquad\qquad\qquad M_{\text{gmag}} := \|\nabla M\| \tag{27}$$

$$\mathbf{P}_{\text{gdir}} := \frac{\nabla P}{\|\nabla P\|} \qquad\qquad\qquad \mathbf{M}_{\text{gdir}} := \frac{\nabla M}{\|\nabla M\|} \tag{28}$$

$$\delta_{\text{dir}}(\mathbf{n}_1, \mathbf{n}_2) := \begin{cases} 1 & \text{if } \langle \mathbf{n}_1, \mathbf{n}_2 \rangle > \arccos(\alpha_{\max}) \\ 0 & \text{else} \end{cases} \tag{29}$$

we can write this similarity score R as

$$R = \frac{\int_{\Omega_c} \delta_{\mathrm{dir}}\left(\mathbf{P}_{\mathrm{gdir}}(\mathbf{x}), \mathbf{M}_{\mathrm{gdir}}(\mathbf{x})\right) \cdot P_{\mathrm{gmag}}(\mathbf{x}) \cdot M_{\mathrm{gmag}}(\mathbf{x}) \, d\mathbf{x}}{\sqrt{\left(\int_{\Omega_c} P_{\mathrm{gmag}}^2(\mathbf{x}) \, d\mathbf{x}\right) \cdot \left(\int_{\Omega_c} M_{\mathrm{gmag}}^2(\mathbf{x}) \, d\mathbf{x}\right)}} \, . \tag{30}$$

Similar to a normalized cross correlation this score ranges from 0 (no similarity) to 1 (perfect similarity). This comparison is computed for all rosette candidates and the resulting scores are written into a detection map (Supplementary Fig. 14e). By applying a threshold of 0.5 to this detection map, only few false positive detections are left. In a subsequent manual post-processing step, we removed remaining false-positive detections and joined detections in consecutive frames that belong to the same rosette.

References

[1] B.B. Avants, C.L. Epstein, M. Grossman, and J.C. Gee. Symmetric diffeomorphic image registration with cross-correlation: Evaluating automated labeling of elderly and neurodegenerative brain. *Medical Image Analysis*, 12(1):26–41, February 2008.

[2] T. Brox, A. Bruhn, N. Papenberg, and J. Weickert. High accuracy optical flow estimation based on a theory for warping. In *European Conference on Computer Vision (ECCV)*, volume 3024 of *Lecture Notes in Computer Science*, pages 25–36. Springer, May 2004.

[3] P. Felzenszwalb and D. Huttenlocher. Distance transforms of sampled functions. Technical Report TR2004-1963, Cornell Computing and Information Science, 2004.

[4] Y. Sato, C.F. Westin, A. Bhalerao, S. Nakajima, N. Shiraga, S. Tamura, and R. Kikinis. Tissue classification based on 3d local intensity structures for volume rendering. *IEEE Transactions on Visualization and Computer Graphics*, 6(2):160–180, 2000.

[5] J. Weickert. *Anisotropic diffusion in image processing*. B.G. Teubner Stuttgart, 1998.